Communications Materials

https://doi.org/10.1038/s43246-026-01255-1

Article in Press

Giant tunable topological Hall effect in $La_{0.7}Sr_{0.3}MnO_3/SrIrO_3$ bilayers

Received: 12 January 2026

Accepted: 19 June 2026

Published online: 27 June 2026

Cite this article as: Peralta-Somoza, A., Lopez, S., Fuster, R. *et al.* Giant tunable topological Hall effect in $La_{0.7}Sr_{0.3}MnO_3/SrIrO_3$ bilayers. *Commun Mater* (2026). https://doi.org/10.1038/s43246-026-01255-1

Andrea Peralta-Somoza, Sandra Lopez, Rafael Fuster, Fernando Gallego, Sergio Valencia, Juan J. Riquelme, Mariona Cabero, Javier Tornos, Carmen Munuera, Federico Mompeán, Mar García-Hernández, Timothy R. Charlton, Brian J. Kirby, Stephan Rosenkranz, Zouhair Sefrioui, Javier E. Villegas, Suzanne G. E. te Velthuis, Carlos León & Jacobo Santamaría

We are providing an unedited version of this manuscript to give early access to its findings. Before final publication, the manuscript will undergo further editing. Please note there may be errors present which affect the content, and all legal disclaimers apply.

If this paper is publishing under a Transparent Peer Review model then Peer Review reports will publish with the final article.

ARTICLE IN PRESS

© The Author(s) 2026. **Open Access** This article is licensed under a Creative Commons Attribution-NonCommercial-NoDerivatives 4.0 International License, which permits any non-commercial use, sharing, distribution and reproduction in any medium or format, as long as you give appropriate credit to the original author(s) and the source, provide a link to the Creative Commons licence, and indicate if you modified the licensed material. You do not have permission under this licence to share adapted material derived from this article or parts of it. The images or other third party material in this article are included in the article's Creative Commons licence, unless indicated otherwise in a credit line to the material. If material is not included in the article's Creative Commons licence and your intended use is not permitted by statutory regulation or exceeds the permitted use, you will need to obtain permission directly from the copyright holder. To view a copy of this licence, visit http://creativecommons.org/licenses/by-nc-nd/4.0/.

ARTICLE IN PRESS

Giant tunable topological Hall effect in $La_{0.7}Sr_{0.3}MnO_3$ / $SrIrO_3$ bilayers

Andrea Peralta-Somoza[1], Sandra Lopez[1], Rafael Fuster[1], Fernando Gallego[1], Sergio Valencia[2], Juan J. Riquelme[3,4], Mariona Cabero[5], Javier Tornos [1], Carmen Munuera[3,4], Federico Mompeán[3,4], Mar García-Hernández[3,4], Timothy R. Charlton[6], Brian J. Kirby[7], Stephan Rosenkranz[8], Zouhair Sefrioui[1], Javier E. Villegas[9], Suzanne G.E. te Velthuis[8], Carlos León[1,4] and Jacobo Santamaría [1,4, #]

[1] *GFMC, Dept. Fisica de Materiales, Facultad de Fisica, U. Complutense, 28040 Madrid, Spain*
[2] *Helmholtz Zentrum Berlin für Materialien und Energie, 12489 Berlin, Germany*
[3] *2D-Foundry Group, I. de Ciencia de Materiales de Madrid ICMM-CSIC, 28049 Madrid, Spain*
[4] *Laboratorio de Heteroestructuras con Aplicación en Espintrónica, ICMM-CSIC, Madrid, Spain*
[5] *ICTS Centro Nacional de Microscopia Electrónica "Luis Brú" Universidad Complutense. 28040 Madrid*
[6] *Neutron Scattering Division, Oak Ridge National Laboratory, Oak Ridge, TN, 37831 USA*
[7] *NIST Center for Neutron Research, National Institute of Standards and Technology, Gaithersburg, Maryland, 20899, USA*
[8] *Materials Science Division, Argonne National Laboratory, Lemont, IL, 60439, USA*
[9] *Laboratoire Albert Fert, CNRS, Thales, Université Paris-Saclay, 91767 Palaiseau, France*

[#] Corresponding author: Jacobo Santamaria (jacsan@fis.ucm.es)

ARTICLE IN PRESS

The topological Hall effect (THE) arises from a Berry phase imprinted on conduction electron spins as they traverse noncollinear magnetic textures. It constitutes a transport hallmark of chiral magnetism. Very large THE signals are theoretically expected in oxide heterostructures combining 3d or 4d ferromagnets and 5d metals with strong spin–orbit coupling. However, experimental realizations have so far yielded only modest signals whose emergence could not be linked to any chiral magnetic texture. Using ultrathin $La_{0.7}Sr_{0.3}MnO_3/SrIrO_3$ bilayers, here we demonstrate a THE that can be switched ON and OFF by the magnetic history, and we establish a direct one-to-one correspondence between the transport anomaly and the emergence—or disappearance—of a chiral magnetic texture at the interface. Further, the associated THE signal is giant, reaching values an order of magnitude larger than observed earlier in analogous systems. Beyond providing a rare, unequivocal evidence for a pure THE, the controllable link between magnetic chirality and the giant Hall signal at oxide interfaces shows a path for engineering reconfigurable conspicuous topological responses, which could impact spintronic sensing and beyond.

INTRODUCTION

Topologically protected spin textures, such as magnetic skyrmions, have attracted considerable interest in recent years, as they can be used as information vectors in low-power information technologies. Spin textures can

ARTICLE IN PRESS

be stabilized by the interplay between exchange interaction, promoting parallel spin alignment, and Dzyaloshinskii-Moriya interaction (DMI)[1,2], an antisymmetric exchange interaction resulting from the combination of inversion symmetry breaking and strong spin-orbit coupling, which twists spin directions. It was initially used to explain the weak ferromagnetism in antiferromagnetic oxides in spin glasses[3] and magnetoelectric coupling in multiferroic perovskite oxides[4]. Later, it was found to be responsible for a variety of noncollinear spin textures in chiral magnets (e.g., spin spirals [5], magnetic skyrmions [6,7], and chiral domain walls [8], etc).

Under the Dzyaloshinskii-Moriya interaction (DMI), real-space noncollinear magnetic textures nucleate with a finite scalar spin chirality $S_i \bullet (S_j \times S_k)$ [9,10] which endows conduction electrons with a Berry phase acquired when their spins couple to the non collinear local spins. This gives rise to the topological Hall effect (THE), an antisymmetric contribution to the transverse resistivity governed by the effective magnetic field 'felt' by conduction electrons [11]. THE has been observed in chiral magnets [12,13], frustrated magnets[14], Heusler alloys[15–17], and also in perovskite oxides[18–20].

In addition to the noncentrosymmetric magnetic single crystals[21], DMI has been demonstrated in multilayers combining materials with heavy elements and ferromagnets. In multilayers, DMI competes with the Heisenberg exchange over atomically short length scales from the interface to twist spins and nucleate non-collinear spin textures, such as spin spirals or skyrmions [22–24]. A net interfacial DMI requires thin films with asymmetric interfaces [24–26], where the asymmetry may be controlled by the layer sequence or induced chemically [27,28] or structurally through strain engineering [29,30]. In this framework, interfaces between correlated oxides are an interesting scenario to explore chiral magnetic textures. In particular, interfaces between 3d (LSMO) or 4d (SRO) magnets and 5d (SIO) oxides[31–38] with strong spin-orbit interaction are acclaimed benchmarks to explore the interplay between topology and correlations, which has been proposed to be the source of large (giant) values of the THE[18]. At oxide interfaces, there are typically charge transfer processes and polar discontinuities which conspire with correlation broken orbital degeneracy to promote noncollinear spin textures[39,40]. Moreover, the atomic control of interface termination enabled by modern oxide epitaxy allows controlling symmetry breaking, which has been recently shown to play a decisive role in the appearance of THE in LMO/SIO superlattices[38].

In this paper, we report a very large THE in LSMO/SIO ultrathin bilayers. Strikingly, this THE is history-dependent, and can be switched ON and OFF in a controlled manner by magnetic-field protocols. Under zero-field-

ARTICLE IN PRESS

cooled conditions, we observe a robust THE *concurrently* with MFM imaging that reveals a spiral spin texture, offering direct evidence of a chiral magnetic state. Under field-cooled conditions, both the spiral texture and the THE vanish. This one-to-one correspondence between transport and magnetic imaging—modulated through magnetic history—is, to our knowledge, *unique* among THE reports and provides the kind of causal link to chiral magnetic states that has been missing in the field.

Taken together, these results provide long-sought evidence that the THE observed at oxide interfaces can serve as a genuine fingerprint of chiral magnetism generated by the interplay between electronic correlations and spin–orbit-driven topology, shedding light on the intensely debated connection between THE and granular spin textures. This interplay has been theoretically anticipated and is currently pursued as a route to programmable functionalities in oxide interfaces. The demonstration that the chiral texture—and thus the topological Hall response—can be externally manipulated and reversibly switched has direct implications for concepts of programmable quantum matter, non-volatile logic, and emerging device paradigms for computing.

RESULTS

Sample growth and structure

We synthesized LSMO/SIO bilayers on $SrTiO_3$ (100) substrates via high-pressure (pure oxygen) sputtering, at elevated temperatures (see Methods), a technique which yielded atomically sharp interfaces.[41] The control of layer thickness is critical due to the short length scale of the interfacial Dzyaloshinskii-Moriya interaction (DMI). The optimal LSMO thickness was fixed at 3.5 nm (approximately 8 unit cells, u.c.), a compromise between being thin enough to ensure the prevalence of DMI and thick enough to avoid suppression of magnetism due to dead layer formation. The choice of 2.4 nm SIO thickness is also large enough to ensure strong spin-orbit interaction, as it has been reported that the DMI interaction can be modulated by the thickness of the SIO layer[42], but small enough to avoid significant current shunting that could suppress the transverse voltage generated in the LSMO. In the following we discuss magnetotransport of a LSMO/SIO bilayer with a top LSMO (3.5 nm) layer and a bottom SIO (2.4 nm) layer, and of a SIO/LSMO bilayer with reversed layer sequence and the same thickness of the individual layers.

ARTICLE IN PRESS

Transport characterization

We measured magnetotransport in a wide range of temperatures (3 K ≤ T ≤ 160 K) and out-of-plane magnetic fields (0-14 T). We first describe measurements of the transverse resistivity ρ_{xy}.

Before describing the results of bilayers, Figure 1a shows the magnetic field dependence of the transverse resistivity of the single LSMO (3.5 nm) control sample. Two different contributions can be identified: the ordinary Hall effect (OHE), linearly dependent on magnetic field with a positive slope as expected from hole-dominated transport, and the step-like anomalous Hall effect (AHE).

The AHE is proportional to the magnetization M_z of the film, and thus it becomes constant when the magnetic field is above saturation. As it can be seen in Figure 1c, AHE is suppressed at low temperatures and increases as the metal-to-insulator transition (MIT) of the manganite is approached. AHE in manganite owes its (topological) origin to real-space spin chirality of non-coplanar localised t_{2g} spin triads building up when MIT is approached, which endows free electrons with a real-space Berry phase through Hund coupling interaction. [43]

ARTICLE IN PRESS

Figure 1b shows the magnetic field dependence of the transverse resistivity measured after zero field cooling ZFC of a bilayer LSMO (3.5 nm) / SIO (2.4 nm) with LSMO on top. Superimposed to manganite-like OHE and AHE

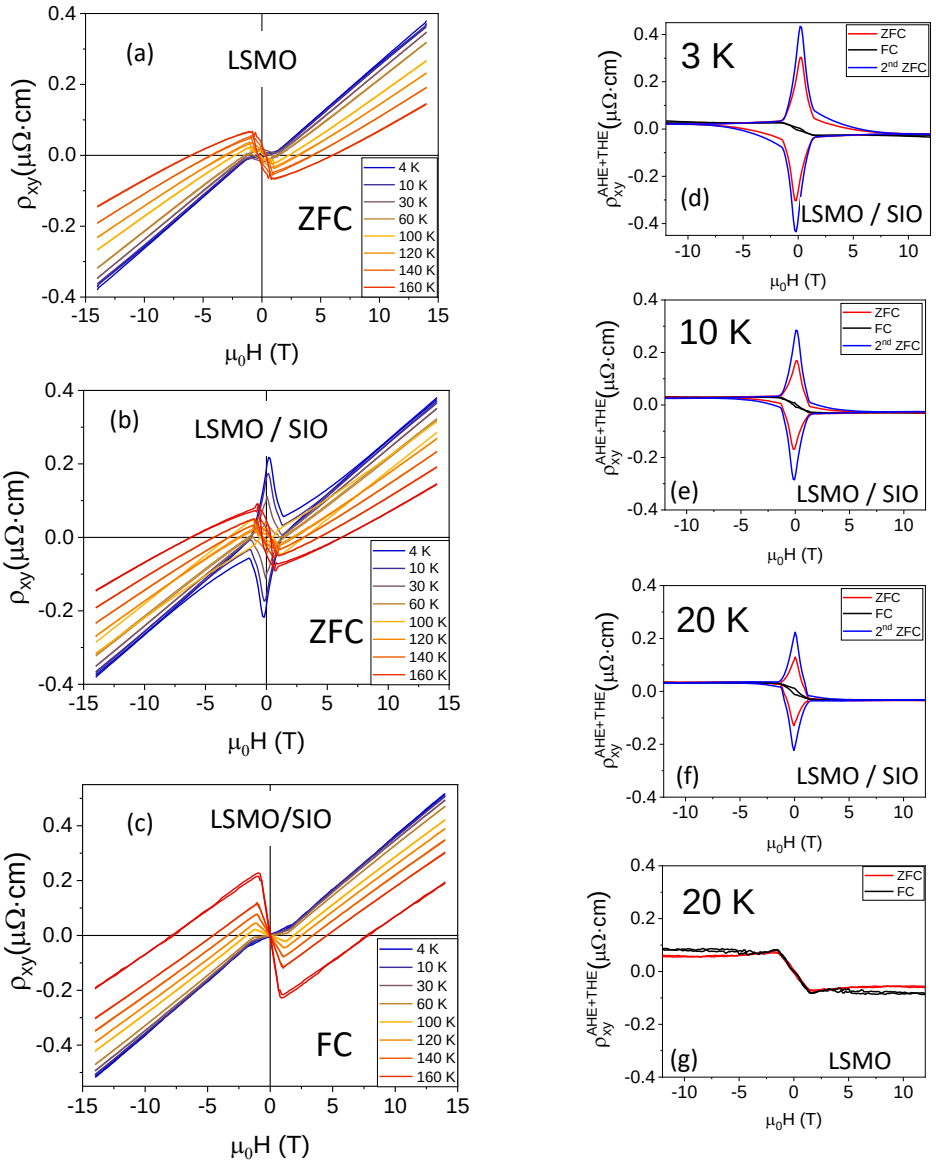

Figure 1. Transport characterisation. (a) Transverse resistivity measurements on a LSMO (3.5 nm) film at 4, 10, 30, 60, 100, 120, 140 and 160 K after a ZFC protocol. (b, c) Transverse resistivity measurements on a LSMO (3.5 nm)/SIO (2.4 nm) bilayer, after a ZFC (b) and FC (c) protocols at the same temperatures. Transverse resistivity after subtracting the linear OHE contribution, for the LSMO (3.5 nm)/SIO (2.4 nm) bilayer, at 3 K (d), 10 K (e), and 20 K (f) and for the LSMO (3.5 nm) film, at 20 K (g). In panels (d) to (g) the initial ZFC measurement (red curve) is followed by a FC measurement (black curve) followed by a second ZFC measurement (blue curve).

components, we observed the emergence of a pronounced antisymmetric peak-shaped component, the topological

ARTICLE IN PRESS

Hall effect (THE). This THE signal is the strongest at low temperatures and decreases sharply when the temperature is increased. Surprisingly, when similar transverse resistivity measurements are performed after field-cooling (FC) in 14 T out-of-plane magnetic fields, the THE nearly vanishes at all temperatures (see Figure 1c), leaving only OHE and AHE contributions. In fact, we found that field-cooling in magnetic fields of 5 T or higher also led to a vanishing THE signal. To more effectively visualize the effect of magnetic history (FC vs ZFC sequence) on the THE and its temperature dependence, Figures 1d-f present transverse resistivity measurements corrected for the OHE contribution, at 3 K, 10 K, and 20 K after a ZFC process (red lines) and after a FC process (black lines). In addition to the THE peak, a strong antisymmetric irreversibility upbuilds up to fields of 7 T, which disappears rapidly when the temperature is increased. Notice also that, after suppressing THE by FC, a subsequent ZFC does recover (with even enhanced values) the THE signal (blue lines). It is important to note that FC or ZFC protocols produced no appreciable changes in the value of the AHE, neither for LSMO/SIO bilayer nor for the LSMO single layer (see Figure 1g). The fact that magnetic history controls the emergence of the THE without affecting AHE suggests a possible connection with (real-space) magnetic textures stabilized preferentially upon cooling in magnetic fields. It is important to stress that the dependence of THE on magnetic history, together with its large values at low temperatures, are important differences compared to previous reports of THE in bilayers of complex oxides [31,38] (see discussion below).

ARTICLE IN PRESS

Interestingly, a SIO/LSMO bilayer with the inverted layer sequence (2.4 nm SIO (top)/ 3.5 nm LSMO (bottom)) did not display the THE peak (See **Supplementary Figure S1**), which, as explained below, provides direct evidence of the interfacial origin of the THE signal.

Magnetic characterization.

To understand the magnetic properties of the interface between strong spin-orbit SIO and ferromagnetic LSMO layer, polarized neutron reflectometry (PNR) experiments were performed on samples with slightly thicker layers. PNR was measured with the incident neutron polarization parallel (R^+) and antiparallel (R^-) to the magnetic field for a (a) SIO (4 nm)(top)/LSMO(5 nm)(bottom) bilayer with a $BiTiO_3$ cap (inverted layer sequence not displaying the THE signal) and (b) LSMO(5 nm)(top)/SIO (4 nm)(bottom) (showing the pronounced THE peak). Samples were field-cooled and measured in a saturating in-plane magnetic field in the 1 T range and at temperatures ranging

ARTICLE IN PRESS

between 20 K to 300 K (See Methods). Plots of the measured and fitted reflectivity curves are displayed in **Supplementary Figure S2** for both samples.

The fits to the data are calculations of the reflectivity based on the scattering length density (SLD) profiles shown in **Figure 2**. For bilayers with SIO on top of the LSMO, the magnetic depth profile shows a strong suppression of magnetism of the LSMO in a 1.3 nm thick layer at the interface (Figure 2a). Instead, bilayers with LSMO on top of the SIO, which exhibit THE, show a slight milder reduction over a thinner 0.6 nm region (Figure 2b) at 20 K.

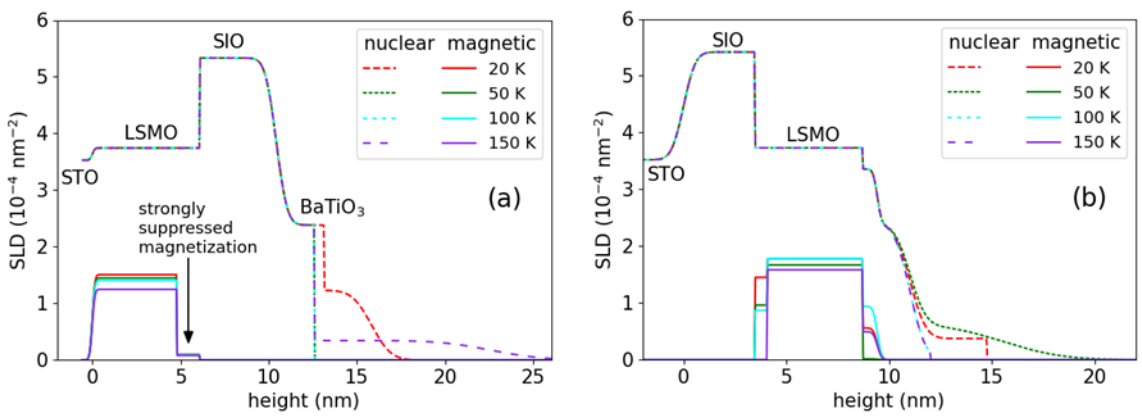

Figure 2. Scattering length density (SLD) profiles from polarized neutron reflectometry. Nuclear and magnetic scattering length density as a function of the height above the STO substrate surface, derived from measurements at 20 K, 50 K, 100 K and 150 K in saturating in-plane magnetic fields, after field cooling, (a) SIO (4 nm)(top)/LSMO(5 nm)(bottom) bilayer with a $BaTiO_3$ cap (b) LSMO(5 nm)(top)/SIO (4nm). The measured reflectivity and fits to the data that corresponds to these SLD profiles are shown in Supplementary Figure S2.

The magnetization in this thin interfacial layer decreases with increasing temperature and is also suppressed at the highest temperature. The different magnetic profile across the interface, and particularly the strongly suppressed magnetization for all temperatures for SIO(top)/LSMO (bottom) samples, may be related to different interface terminations for both layer sequences, with excess SrO planes at the interface[41], which have a doping effect at the interfacial LSMO as shown by STEM EELS experiments[44]. While for the LSMO (top)/SIO interface the Mn oxidation state is 3.3 as expected from the stoichiometry, in the case of the SIO (top)/LSMO sample Mn attains a 3.5 oxidation state at the interface, which renders the interfacial layer non-ferromagnetic. The suppression of THE in the presence of the ~1 nm thick interfacial layer with strongly suppressed magnetization demonstrates its interfacial origin and strongly points to the very short length scale DM interaction being at its origin.

ARTICLE IN PRESS

SQUID magnetometry experiments were performed to investigate the effects of zero-field cooling (ZFC) and field cooling (FC) on the system. We conducted measurements of magnetization as a **Figure 3 SQUID measurements**.

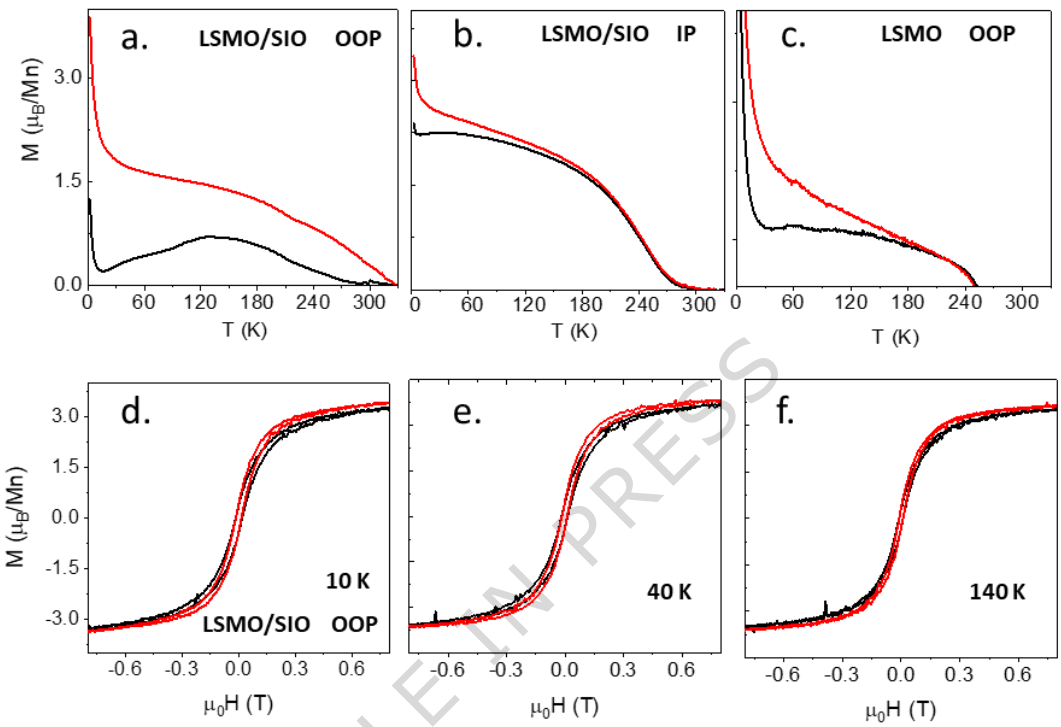

FC at 0.1 T (red lines) and ZFC (black lines) Magnetisation as a function of temperature of a LSMO (3.5 nm) / SIO (2.4 nm) bilayer measured in (a) out-of-plane (OOP)and (b) in-plane (IP) 0.1 T magnetic fields. (c) Magnetisation as a function of temperature of a LSMO (3.5 nm) control sample. (d)-(f) M(H) loops of a LSMO (3.5 nm) / SIO (2.4 nm) bilayer at 10, 40 and 140 K.

function of temperature for both ZFC and FC cases as presented in Figures 3a and 3b. The measuring field and FC fields were 0.1 T.

While there are no significant differences between ZFC and FC for in-plane magnetization, major differences are observed for out-of-plane magnetization. Upon ZFC, the out-of-plane magnetization is strongly suppressed at low temperatures, indicating a blocking, which is not observed after FC and is also absent in single LSMO layers (see panel c). Magnetization loops of LSMO/SIO bilayers measured in out-of-plane magnetic fields after FC and ZFC cooling protocols showed only minor differences in the saturation magnetization (ZFC showed a 4% reduction of the saturation magnetization as compared to FC at 10 K). This very minor difference is further reduced as the temperature is increased, almost vanishing at 140 K where the THE signal is absent (see panels d –

ARTICLE IN PRESS

f in Figure 3). Considering the above, it becomes clear that the THE signal, which shows in the LSMO/SIO bilayers for fields well beyond the saturation field (up to 7 T, see Figure 1), does not correlate with the major magnetic features displayed by the M(H) loops. In other words, the THE signal is driven by a minor magnetic volume fraction.

Magnetic Force Microscopy (MFM)

In an effort to further elucidate the relationship between THE and the magnetic texture, we carried out MFM imaging of the LSMO/SIO bilayer in out-of-plane applied magnetic fields. See Figure 4. In this experiment, (phase contrast) magnetization images were obtained after ZFC and FC down to 17 K (the base temperature of our MFM experiment) and in strong out of plane magnetic fields (5T), a field range in which magnetometry indicates that film is mostly saturated (see Fig. 3), a striking difference appears between ZFC and 5T FC sequences. In the ZFC sequence, although, according to magnetometry experiments described above, at 5 T the magnetization is mostly saturated, distinct inclined stripes can be recognized (see Figure 4a), which do not correspond to topographical features (as shown by the atomic force microscopy, AFM, image displayed in Figure 4b with a roughness well below 1 nm as illustrated in **Supplementary Figure S3**). The contrast modulation of the mentioned stripes corresponds to spin spirals where magnetization changes direction from out of plane (blue) to into the plane (red) over hundreds of nm wide distances. Since MFM contrast scales with intensity of the sample's magnetic stray field gradient, the weak contrast indicates that the spin spiral phase corresponds to a small volume fraction of the magnetic sample, the saturated (main) part of the sample not contributing to the signal.

Interestingly, spirals disappear when the FC protocol is conducted in magnetic fields of 5T or higher. Figure 4c shows an MFM image of the sample at 17 K and in 5T field after FC, showing the weak contrast expected for a saturated sample. The AFM topographic image of Figure 4d also shows essentially no contrast. Notice that although the topographic images acquired simultaneously with the MFM data at 17 K and 5 T have somewhat reduced spatial resolution, a topographic image of the same sample measured at room temperature and zero field using a non-magnetic super-sharp probe, **see Supplementary Figure S3,** also shows a very low roughness (~0.5 nm), consistent with the one obtained at low temperature. Within this sensitivity, no clear spatial correlation is observed between the MFM contrast and the AFM topography.

ARTICLE IN PRESS

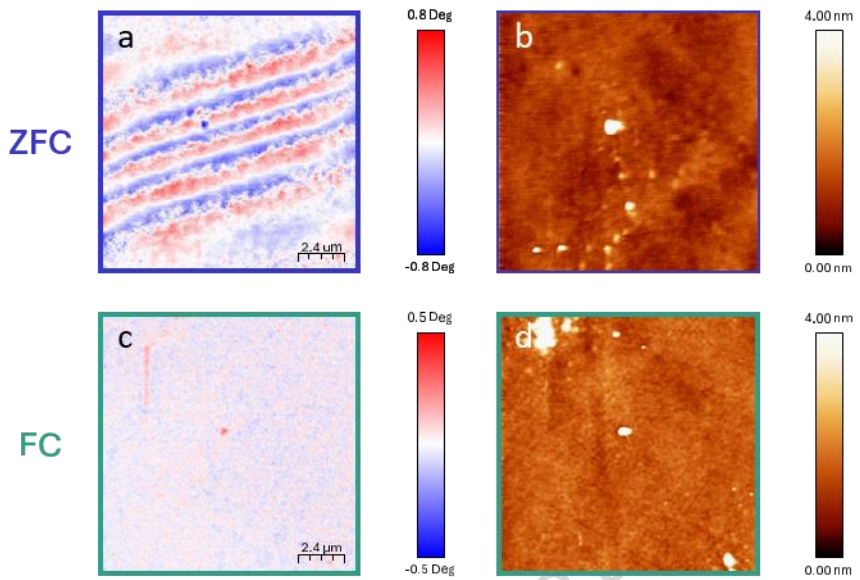

Figure 4 Magnetic force microscopy MFM images a,c) (Phase contrast) MFM images of a LSMO (3.5 nm)/SIO (2.4 nm) bilayer taken at 17 K in 5T fields applied out of plane after ZFC (a) and FC in a 5T magnetic field (c). Panels b and d show the corresponding AFM topography images.

The effect of magnetic field sweeps on the magnetic texture of the same bilayer is illustrated in Figure 5. The first row shows measurements after a ZFC sequence, and the second row after FC. MFM images for magnetic fields below 1T (which nearly corresponds to the saturation field observed in SQUID magnetometry) evidence a coarse magnetic texture with small grains. This is the magnetic field range where the THE peak is observed. However, we cannot ascribe the origin of the THE to the small magnetic grains only, since both ZFC (featuring THE) and FC (with absent THE) sequences display similar grains. Yet, in the ZFC case (upper row in Figure 5) the spirals' contrast can be identified superimposed to that of magnetic grains within the magnetic field interval where the large THE peak is observed. Moreover, spirals are not observed when temperature is increased above the temperature where THE disappears, indicating that there is a direct connection between THE peaks and the spiral texture (**See Supplementary Figure S4**). Interestingly, at low temperatures, the antisymmetric irreversibility in the transverse resistivity characteristic of THE persists at larger magnetic fields, where only spirals and no magnetic grains are observed in MFM images. See transverse resistivity loops of Figure 1. Notice that the granular magnetic

ARTICLE IN PRESS

structure and the spirals persist at magnetic fields where the magnetization is nearly saturated according to magnetometry (Fig. 3), indicating that both correspond to a minority volume fraction of the magnetic phase.

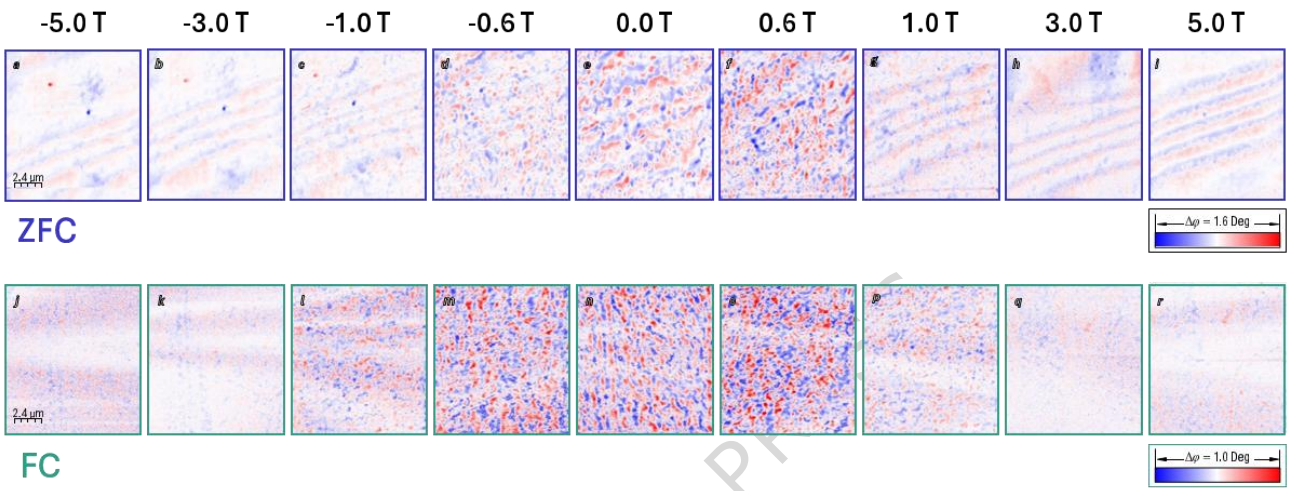

Figure 5. Evolution the magnetic textures with the magnetic field. MFM images of a LSMO (3.5 nm)/SIO (2.4 nm) bilayer taken at 17 K and in different magnetic fields between -5T to 5 T after a ZFC (upper panels) and after a FC in 5T fields (bottom panels).

Considering the above, it is clear that the spiral spin texture is a key ingredient for the observation of THE. Yet, comparing Figures 1 and 5, it becomes apparent that the largest THE signal occurs in a magnetic field range where the granular magnetic structure is observed. We argue below that the granular magnetic structure, although not sufficient on its own to observe the THE signal, also plays an important role. This is further supported by the magnetoresistance measurements shown in **Supplementary Figures S5,** as well as the magnetic imaging by MFM (**Supplementary Fig. S6)** and magneto-optical images in **Supplementary Fig. S7** sensitive to in-plane moments**.**

Supplementary Figures S5 (a) and **(b)** show that, regardless of the FC or ZFC protocol, the LSMO/SIO bilayer presents an anomalous low-temperature magnetoresistance: notice the large low-temperature MR, in excess of 50%, which decreases when the temperature is increased. This is at odds with the case of ultrathin manganite single layers and SIO/LSMO bilayer with the inverted layer sequence (SIO layer on top), which both display a weaker low-temperature MR ~ 10% that increases as the temperature is increased (**Supplementary Figure S5 (c) and (d)**. Because the LSMO/SIO bilayer presents a granular ferromagnetic state that is absent in the case of ultrathin manganite films (see **Supplementary Figures S6** and **S7** showing both large magnetic domains for the single

ARTICLE IN PRESS

LSMO layer**),** the anomalous MR must be caused by the granular ferromagnetic state. Within the double exchange transport scenario, the large MR is indeed well explained by the spin noncollinearity typical of a granular magnetic structure. In this scenario, FC and ZFC produced no significant differences in the low-temperature magnetoresistance because, as seen by MFM magnetic imaging, the low-field granular magnetic structure is present regardless of the magnetic history. Since the anomalous MR is exactly similar for ZFC and FC cases we conclude that the spiral magnetic texture has no impact on the longitudinal resistance, yet it has a strong impact on the transverse resistance. This, again, indicates that the THE probes the chiral property of the interface. The similar MR behavior of inverted SIO(top)/LSMO(bottom) and single LSMO films is consistent with the expectation that the strongly suppressed magnetism over ~1 nm in the LSMO at the interface quenches the effect of the DMI interaction on the LSMO at the interface, preventing also the trigger of the granular magnetic texture. The suppressed magnetism at the SIO(top)/LSMO(bottom) interface denounced by the PNR experiment has been recently confirmed by XMCD from the suppression of the induced moment at the interfacial Ir due to superexchange interaction with the Mn at the LSMO side[44]. The picture emerges that the magnetic "host" for the texture is simply missing. Accordingly, both layers of the SIO (top) /LSMO (bottom) sample are decoupled, and, as a result, it behaves magnetically akin to a single LSMO layer. In summary, it becomes apparent that the magnetic granularity of the LSMO (top)/SIO sample also has an interfacial origin, and most likely, as the spirals, it is also localized in the close vicinity of the interface with a small magnetic volume fraction as denounced by SQUID magnetometry.

Contrary to previous works [2,5,9], where THE is related to the observation of granular magnetic structure (typically ascribed to magnetic textures of aggregated skyrmions), in our experiments the magnetic granularity is observed both in FC and ZFC measurements. This implies that the granularity cannot by itself explain the observed THE. This must be linked to the presence of the spiral texture, which only nucleates in ZFC. It has been shown theoretically[42] that spin spirals emerging at the interface between ferromagnets and heavy metals are the precursors of skyrmion phases typically featuring THE. In particular, the spiral state results from the competition between the Dzyaloshinskii-Moriya interaction (DMI) ferromagnetic (FM) exchange and magnetic anisotropy. An increased strength of the DMI –or conversely by a decrease of the FM exchange interaction strength[42]– favours a spin-spiral

ARTICLE IN PRESS

phase[39,45], which may evolve into a skyrmion crystal in the presence of magnetic fields[7,46–49]. A lower bound of the DMI interaction responsible for the spiral ground-state observed upon ZFC (MFM imaging in Figs. 4 and 5) can be estimated from the spiral period $T \sim 4\pi \frac{A}{D}$ expected [50]in the limit of small anisotropy, with A and D being the exchange stiffness and the DMI, respectively. In view of the period $T \sim 2\mu m$ observed for the spirals, and using typical values of $A = 1\ pJm^{-1}$ for the manganites [51], values of D result in the order $D \sim 6\ \mu Jm^{-2}$. The formation of the spiral texture happens only after ZFC, where the weakened FM state at temperatures close to the LSMO's Curie temperature tips the balance between exchange and DMI. In contrast, in the FC sequence, the Zeeman energy term promotes a ferromagnetic ground state. It is surprising, though, that once the spiral state is stabilized upon ZFC, it remains robust against very large magnetic fields (high Zeeman energy). Even considering that at the interface the Mn moment is halved with respect to the bulk of LSMO (see Fig. 2), the Zeeman energy $\sim BM_S$ (with M_S the saturation magnetization) for fields as high as 5 T greatly exceeds the DMI energy $\sim 2\pi D/L$.[52] This indicates that the spiral state is metastable under such applied fields, and that a large activation energy must exist hindering the spiral unwinding. The origin of this energy barrier remains speculative at this point and may involve magnetic pinning by defects.

When the spiral phase nucleates at the interface due to the alluded competition between the DMI with FM exchange, a large THE signal is observed, evidencing the causal link between spiral state and THE. In the FC sequence spirals are absent, and THE is, in consequence, not observed. Yet, since the maximal THE signal appears in a magnetic field range where both the granular magnetic structure and the spiral contrast are observed, it is reasonable to think that both spirals and magnetic granularity play a role in the large THE peaks observed in our system.

A statistical analysis of the coarse-grained magnetic texture observed both in FC and ZFC (see central images of Figure 5) evidences an average magnetic domain diameter of ~400 nm, one order of magnitude larger than the estimate of the skyrmion size that can be calculated from the amplitude of the THE peak according to the Bruno formula[11]. Following Bruno, the THE results from the Berry phase acquired by the electron as it moves in the spatially varying spin texture. In this simple model for strong ferromagnetic exchange coupling, the THE then takes a value given by

$$\rho_{THE} = \frac{P\langle b \rangle}{en} = \frac{\Phi_0 n_{sk} P}{en} = \Phi_0 n_{sk} P R_0$$

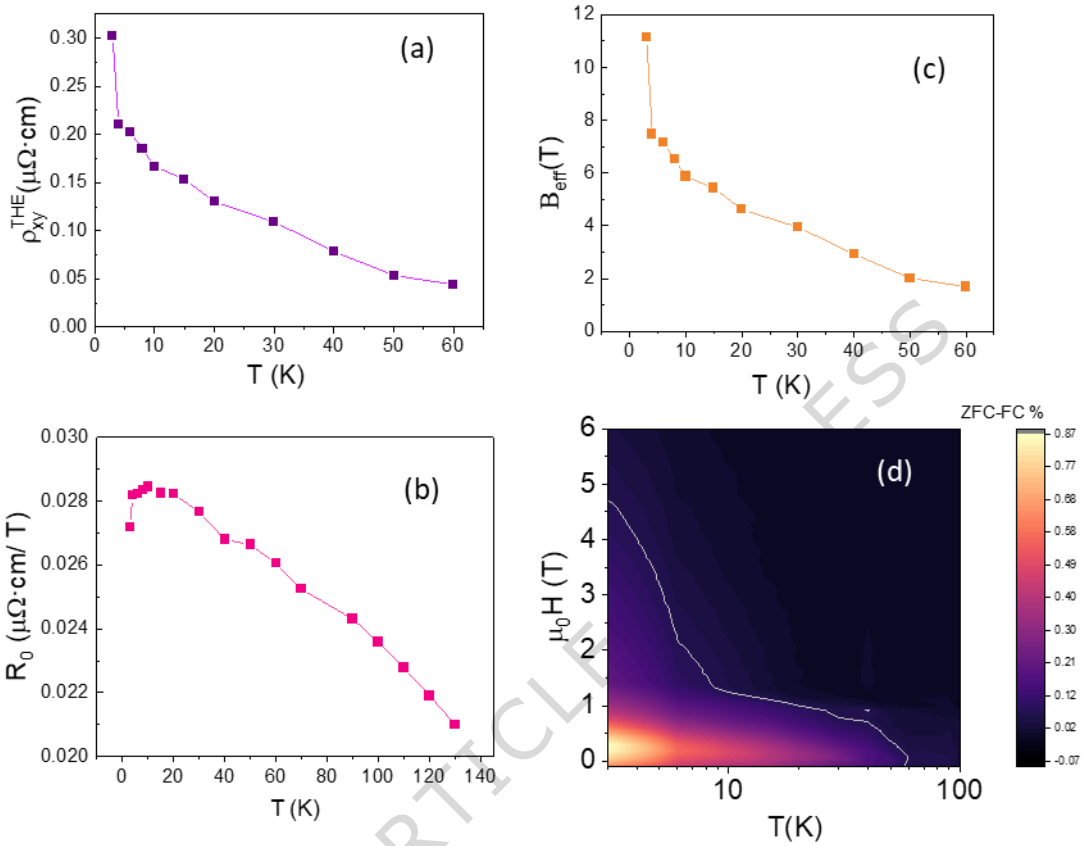

Figure 6. Analysis of the temperature dependence of the THE. Temperature dependence of (a) THE signal at its maximum value ρ_{xy}^{THE}, (b) (ordinary) Hall resistance R_0 (c) effective magnetic field $B_{eff}=\rho_{xy}^{THE}/R_0$. (d) Magnetic field-temperature phase diagram of the THE signal measured as % change of ZFC -FC signal relative to the low temperature ZFC maximum value.

where P is the spin polarization, e is the electron charge, n is the charge density and R_0 is the Hall resistivity and $\boldsymbol{b}$ is an effective (emergent) perpendicular magnetic field that originates the THE. The amplitude of $\boldsymbol{b}$ depends on the topology of the spin textures through the skyrmion density $\langle b \rangle =$

$\Phi_0 n_{sk}$ where Φ_0 is the flux quantum and n_{sk} the average skyrmion density carrying a topological charge Q = 1. Inserting into this expression the experimental values of the THE and Hall resistivity (see Fig. 1b), skyrmion diameters in the range 20 – 50 nm are obtained, much smaller than the values obtained for the granular small features from the analysis of the experimental images ~ 400 nm.

ARTICLE IN PRESS

Discrepancies in the skyrmion densities obtained from THE and MFM have been observed before and have fuelled the growing debate on the connection between electronic transport phenomena and chiral magnetism [11,53,54]. While in some cases THE has been found to scale with the skyrmion density[12,33,34,55], this is not the case in magnetic multilayers where large discrepancies between the skyrmion densities obtained from THE and MFM have been reported. In particular, discrepancies comparable to those we find in this work have been found in magnetic oxide films[10,28] and multilayers[2]. Part of these departures can be accounted for by skyrmion-bubbles[6,56], chiral magnetic (bubble) domains stabilized by the dipolar interaction and with a THE akin to skyrmions as they possess the same skyrmion number[53]. However, the THE dependence on the magnetic history and the large size (compared to expected skyrmion size) of the granular magnetic features observed in MFM images, both after FC and ZFC, suggests that, rather than conventional skyrmions, here the THE may be caused by chiral domain walls of small magnetic domains. The picture emerges that the spirals endow the boundaries of the small magnetic grains with a chiral structure responsible for the THE.

The evolution of the THE signal with temperature is also anomalous. The amplitude of the THE peak, $\rho_{,xy}^{THE}$, decreases strongly when the temperature is increased (Figure 6a). This is not expected for magnetic skyrmions[11] which yield an essentially temperature-independent THE. The THE decrease upon temperature increase may be related to the observed depression of interfacial LSMO layer (0.6nm thick) magnetization as measured with PNR. See Figure 2. Due to the short range of the DMI, a reduced interfacial magnetization explains the reduced THE signal. In agreement with this argument, Supplementary Figure S5 shows the disappearance of the spiral texture when temperature is increased. Moreover, the enhancement of THE at low temperature rules out the connection with fluctuating non-collinear spins, known to be present in manganites at the MIT. It is important to notice here that in previous reports of THE in SIO/LSMO multilayers [31], the maximal THE is observed at temperatures of 200 K, indicating a different origin than in the case of the bilayers studied here. Our case is also very different from the THE reported for (LMO)/(SIO) superlattices [38], where its magnitude is comparable to AHE. In contrast, in our system the THE can be one order of magnitude larger than the AHE. See **Supplementary Table 1 and Supplementary Figure S8**. Notice that although AHE and THE have different origins (AHE is due to topological properties of electronic states in momentum space while THE is due to spin textures in real space), their

ARTICLE IN PRESS

ratio is relevant insofar the THE is better observed in samples with small relative values of the AHE. Using the Hall coefficient R_0 (Figure 6b) we calculate the effective magnetic field B_{eff} associated to the THE. As shown in **Figure 6c**, B_{eff} values are small compared to those observed typically in skyrmion systems. **Figure 6d** shows the distribution of the THE phase in a magnetic field-temperature parameter space. The contour plot shows the relative excess of the THE transverse resistivity $\frac{\rho_{xy}^{ZFC}-\rho_{xy}^{FC}}{\rho_{xy}^{ZFC}}$. Notice that apart of the THE peak at low field, there is an antisymmetric contribution at high field probably driven by the spiral phase.

A last comment regards recent papers where the interpretation of THE as the transport signature of chiral spin textures has been challenged[57–61] mostly in connection to experiments on $SrRuO_3$ (SRO) oxide interfaces showing that, in addition, intrinsic (momentum space) electronic mechanisms and/or inhomogeneities may yield a multicomponent anomalous Hall effect, whose superposition can be mistaken with THE[61]. As opposed to the case of $SrRuO_3$ where AHE components with different signs have been reported, Hall effect measurements of ultrathin manganites yielded, in all cases, negative AHE. Thus, extrinsic THE-like contributions to the transverse resistivity caused by the superposition of AHE contributions of different sign[53–57] can be ruled out in our system. We conclude that the large THE signal observed in this work, which can be more than one order of magnitude larger than the AHE, is an intrinsic effect.

CONCLUSION

In summary, we have found a large THE signal in LSMO/SIO bilayers with ultrathin individual layers which can be one order of magnitude larger that the manganite's AHE. It can be turned on and off by the magnetic history: THE is observed after ZFC sequence while it is absent after FC. Concurrent with THE, MFM imaging has revealed a chiral magnetic texture which, according to polarized neutron reflectometry experiments, is confined to the interface and appears to play a key role for the observation of the THE. The origin of the chiral magnetic texture is the competition between the DMI prompted at the interface by the strong spin-orbit SIO and the ferromagnetic exchange of the LSMO. These results illustrate the potential of the interplay between topology and correlation at complex oxide interfaces to manipulate chiral magnetic textures and sense them with large transverse resistivity responses, which may prompt novel device functionalities in magnetic sensing and information processing.

ARTICLE IN PRESS

REFERENCES

1. Dzyaloshinsky, I. A thermodynamic theory of "weak" ferromagnetism of antiferromagnetics. *Journal of Physics and Chemistry of Solids* **4**, 241–255 (1958).
2. Moriya, T. Anisotropic Superexchange Interaction and Weak Ferromagnetism. *Physical Review* **120**, 91 (1960).
3. Fert, A. & Levy, P. M. Role of Anisotropic Exchange Interactions in Determining the Properties of Spin-Glasses. *Phys. Rev. Lett.* **44**, 1538 (1980).
4. Sergienko, I. A. & Dagotto, E. Role of the Dzyaloshinskii-Moriya interaction in multiferroic perovskites. *Phys. Rev. B Condens. Matter Mater. Phys.* **73**, 094434 (2006).
5. Bode, M. *et al.* Chiral magnetic order at surfaces driven by inversion asymmetry. *Nature 2007 447:7141* **447**, 190–193 (2007).
6. Jiang, W. *et al.* Blowing magnetic skyrmion bubbles. *Science (1979).* **349**, 283–286 (2015).
7. Mühlbauer, S. *et al.* Skyrmion lattice in a chiral magnet. *Science (1979).* **323**, 915–919 (2009).
8. Ryu, K. S., Thomas, L., Yang, S. H. & Parkin, S. Chiral spin torque at magnetic domain walls. *Nat. Nanotechnol.* **8**, 527–533 (2013).
9. Onoda, M., Tatara, G. & Nagaosa, N. Anomalous Hall Effect and Skyrmion Number in Real and Momentum Spaces. *https://doi.org/10.1143/JPSJ.73.2624* **73**, 2624–2627 (2013).
10. Yi, S. Do, Onoda, S., Nagaosa, N. & Han, J. H. Skyrmions and anomalous Hall effect in a Dzyaloshinskii-Moriya spiral magnet. *Phys. Rev. B Condens. Matter Mater. Phys.* **80**, 054416 (2009).
11. Bruno, P., Dugaev, V. K. & Taillefumier, M. Topological Hall effect and Berry phase in magnetic napostructures. *Phys. Rev. Lett.* **93**, 096806 (2004).
12. Neubauer, A. *et al.* Topological hall effect in the a phase of MnSi. *Phys. Rev. Lett.* **102**, 186602 (2009).
13. Kanazawa, N. *et al.* Large topological hall effect in a short-period helimagnet MnGe. *Phys. Rev. Lett.* **106**, 156603 (2011).
14. Taguchi, Y., Oohara, Y., Yoshizawa, H., Nagaosa, N. & Tokura, Y. Spin chirality, Berry phase, and anomalous Hall effect in a frustrated ferromagnet. *Science* **291**, 2573–2576 (2001).
15. Rana, K. G. *et al.* Observation of topological Hall effect in Mn2RhSn films. *New J. Phys.* **18**, 085007 (2016).
16. Swekis, P. *et al.* Topological Hall effect in thin films of ${\rm Mn}_{1.5} {\rm PtSn}$. *Phys. Rev. Mater.* **3**, 13001 (2019).
17. Vir, P. *et al.* Anisotropic topological Hall effect with real and momentum space Berry curvature in the antiskrymion-hosting Heusler compound Mn1.4 PtSn. *Phys. Rev. B* **99**, 140406 (2019).

ARTICLE IN PRESS

18. Vistoli, L. *et al.* Giant topological Hall effect in correlated oxide thin films. *Nat. Phys.* **15**, 67–72 (2019).

19. Nakamura, M. *et al.* Emergence of Topological Hall Effect in Half-Metallic Manganite Thin Films by Tuning Perpendicular Magnetic Anisotropy. *https://doi.org/10.7566/JPSJ.87.074704* **87**, (2018).

20. Wang, W. *et al.* Spin chirality fluctuation in two-dimensional ferromagnets with perpendicular magnetic anisotropy. *Nat. Mater.* **18**, 1054–1059 (2019).

21. Shibata, K. *et al.* Large anisotropic deformation of skyrmions in strained crystal. *Nature Nanotechnology 2015 10:7* **10**, 589–592 (2015).

22. Moreau-Luchaire, C. *et al.* Additive interfacial chiral interaction in multilayers for stabilization of small individual skyrmions at room temperature. *Nature Nanotechnology 2016 11:5* **11**, 444–448 (2016).

23. Dupé, B., Bihlmayer, G., Böttcher, M., Blügel, S. & Heinze, S. Engineering skyrmions in transition-metal multilayers for spintronics. *Nature Communications 2016 7:1* **7**, 1–6 (2016).

24. Heinze, S. *et al.* Spontaneous atomic-scale magnetic skyrmion lattice in two dimensions. *Nature Physics 2011 7:9* **7**, 713–718 (2011).

25. Fert, A. R. Magnetic and Transport Properties of Metallic Multilayers. *Materials Science Forum* **59–60**, 439–480 (1990).

26. Romming, N. *et al.* Writing and deleting single magnetic skyrmions. *Science* **341**, 636–639 (2013).

27. Chen, G. *et al.* Large Dzyaloshinskii-Moriya interaction induced by chemisorbed oxygen on a ferromagnet surface. *Sci. Adv.* **6**, (2020).

28. Kim, D. H. *et al.* Bulk Dzyaloshinskii-Moriya interaction in amorphous ferrimagnetic alloys. *Nat. Mater.* **18**, 685–690 (2019).

29. Davydenko, A. V. *et al.* Dzyaloshinskii-Moriya interaction in symmetric epitaxial [Co/Pd(111)]N superlattices with different numbers of Co/Pd bilayers. *Phys. Rev. B* **99**, 014433 (2019).

30. Zhang, W. *et al.* Tunable interfacial Dzyaloshinskii–Moriya interaction in symmetrical Au/[Fe/Au]n multilayers. *Nanoscale* **13**, 2665–2672 (2021).

31. Li, Y. *et al.* Emergent Topological Hall Effect in La0.7Sr0.3MnO3/SrIrO3 Heterostructures. *ACS Appl. Mater. Interfaces* **11**, 21268–21274 (2019).

32. Yia, D. *et al.* Atomic-scale control of magnetic anisotropy via novel spin-orbit coupling effect in La2/3Sr1/3MnO3/SrIrO3 superlattices. *Proc. Natl. Acad. Sci. U. S. A.* **113**, 6397–6402 (2016).

33. Matsuno, J. *et al.* Interface-driven topological Hall effect in SrRuO3-SrIrO3 bilayer. *Sci. Adv.* **2**, (2016).

34. Ohuchi, Y. *et al.* Electric-field control of anomalous and topological Hall effects in oxide bilayer thin films. *Nature Communications 2018 9:1* **9**, 1–7 (2018).

ARTICLE IN PRESS

ARTICLE IN PRESS

35. Nichols, J. *et al.* Emerging magnetism and anomalous Hall effect in iridate–manganite heterostructures. *Nature Communications 2016 7:1* **7**, 1–6 (2016).

36. Okamoto, S. *et al.* Charge Transfer in Iridate-Manganite Superlattices. *Nano Lett.* **17**, 2126–2130 (2017).

37. Yoo, M. W. *et al.* Large intrinsic anomalous Hall effect in SrIrO3 induced by magnetic proximity effect. *Nature Communications 2021 12:1* **12**, 1–9 (2021).

38. Skoropata, E. *et al.* Interfacial tuning of chiral magnetic interactions for large topological Hall effects in LaMnO3/SrIrO3 heterostructures. *Sci. Adv.* **6**, (2020).

39. Banerjee, S., Erten, O. & Randeria, M. Ferromagnetic exchange, spin–orbit coupling and spiral magnetism at the LaAlO3/SrTiO3 interface. *Nature Physics 2013 9:10* **9**, 626–630 (2013).

40. Nandy, A. K., Kiselev, N. S. & Blügel, S. Interlayer Exchange Coupling: A General Scheme Turning Chiral Magnets into Magnetic Multilayers Carrying Atomic-Scale Skyrmions. *Phys. Rev. Lett.* **116**, 177202 (2016).

41. Yoo, M. W. Large intrinsic anomalous Hall effect in SrIrO3 induced by magnetic proximity effect. *Nat. Commun.* **12**, 1–9.

42. Mohanta, N., Dagotto, E. & Okamoto, S. Topological Hall effect and emergent skyrmion crystal at manganite-iridate oxide interfaces. *Phys. Rev. B* **100**, 064429 (2019).

43. Lyanda-Geller, Y. *et al.* Charge transport in manganites: hopping conduction, the anomalous Hall effect, and universal scaling. *Phys. Rev. B* **63**, 184426 (2001).

44. Peralta-Somoza Andrea et al. Interface magnetism and anomalous Hall effect in La0.7 Sr0.3Mn O3/SrIr O3 bilayers. *Phys. Rev. Mater.* **9**, (2025).

45. Li, X., Liu, W. V. & Balents, L. Spirals and skyrmions in two dimensional oxide Heterostructures. *Phys. Rev. Lett.* **112**, 067202 (2014).

46. Ezawa, M. Compact merons and skyrmions in thin chiral magnetic films. *Phys. Rev. B Condens. Matter Mater. Phys.* **83**, 100408 (2011).

47. Huang, S. X. & Chien, C. L. Extended skyrmion phase in epitaxial FeGe(111) thin films. *Phys. Rev. Lett.* **108**, 267201 (2012).

48. Yu, X. Z. *et al.* Biskyrmion states and their current-driven motion in a layered manganite. *Nat. Commun.* **5**, (2014).

49. Bogdanov, A. & Hubert, A. Thermodynamically stable magnetic vortex states in magnetic crystals. *J. Magn. Magn. Mater.* **138**, 255–269 (1994).

50. Rößler, U. K., Leonov, A. A. & Bogdanov, A. N. Chiral Skyrmionic matter in non-centrosymmetric magnets. *J. Phys. Conf. Ser.* **303**, 012105 (2011).

51. Nagai, T. *et al.* Direct observation of the spin structures of vortex domain walls in ferromagnetic nanowires. *Phys. Rev. B* **78**, 180414 (2008).

ARTICLE IN PRESS

ARTICLE IN PRESS

52. Hervé, M. *et al.* Stabilizing spin spirals and isolated skyrmions at low magnetic field exploiting vanishing magnetic anisotropy. *Nature Communications 2018 9:1* **9**, 1015- (2018).

53. Nagaosa, N. & Tokura, Y. Topological properties and dynamics of magnetic skyrmions. *Nature Nanotechnology 2013 8:12* **8**, 899–911 (2013).

54. Fert, A., Reyren, N. & Cros, V. Magnetic skyrmions: advances in physics and potential applications. *Nat. Rev. Mater.* **2**, 17031 (2017).

55. Raju, M. *et al.* The evolution of skyrmions in Ir/Fe/Co/Pt multilayers and their topological Hall signature. *Nature Communications 2019 10:1* **10**, 1–7 (2019).

56. Malozemoff, A. P. . & Slonczewski, J. C. . *Magnetic Domain Walls in Bubble Materials*. (Academic Press, 1979).

57. Gerber, A. Interpretation of experimental evidence of the topological Hall effect. *Phys. Rev. B* **98**, 214440 (2018).

58. Kimbell, G. *et al.* Two-channel anomalous Hall effect in SrRuO3. *Phys. Rev. Mater.* **4**, 054414 (2020).

59. Wang, L. *et al.* Controllable Thickness Inhomogeneity and Berry Curvature Engineering of Anomalous Hall Effect in SrRuO3 Ultrathin Films. *Nano Lett.* **20**, 2468–2477 (2020).

60. Groenendijk, D. J. *et al.* Berry phase engineering at oxide interfaces. *Phys. Rev. Res.* **2**, 023404 (2020).

61. Kimbell, G., Kim, C., Wu, W., Cuoco, M. & Robinson, J. W. A. Challenges in identifying chiral spin textures via the topological Hall effect. *Communications Materials 2022 3:1* **3**, 1–18 (2022).

62. Horcas, I. *et al.* WSXM: a software for scanning probe microscopy and a tool for nanotechnology. *Rev. Sci. Instrum.* **78**, (2007).

63. Björck, M. & Andersson, G. GenX: An extensible X-ray reflectivity refinement program utilizing differential evolution. *J. Appl. Crystallogr.* **40**, 1174–1178 (2007).

64. Glavic, A. & Björck, M. GenX 3: The latest generation of an established tool. *J. Appl. Crystallogr.* **55**, 1063–1071 (2022).

65. Parratt, L. G. Surface Studies of Solids by Total Reflection of X-Rays. *Physical Review* **95**, 359 (1954).

[&] Certain commercial products or company names are identified here to describe our study adequately. Such identification is not intended to imply recommendation or endorsement by the National Institute of Standards and Technology

ARTICLE IN PRESS

METHODS

Sample fabrication

Epitaxial bilayers of $La_{0.7}Sr_{0.3}MnO_3$ and $SrIrO_3$ were deposited on $SrTiO_3$(001) substrates by high-pressure sputtering. $La_{0.7}Sr_{0.3}MnO_3$ and $SrIrO_3$ were grown on different sputtering setups, minimising transferring time below 2 min. The substrate temperatures (T_s) and the oxygen pressure (PO_2) during the deposition were 650 °C and 284 Pa for $SrIrO_3$ and 900 °C and 324 Pa for $La_{0.7}Sr_{0.3}MnO_3$. Post-deposition, a one-hour annealing was performed at T_s =650°C and P_{O2} = 93200 Pa for $SrIrO_3$ and at T_s = 800°C and P_{O2} = 91200 Pa for $La_{0.7}Sr_{0.3}MnO_3$.

Electrical characterization

Transport properties were measured using a Quantum Design Physical Properties Measurement System (PPMS) [&]. The resistances are defined as R_{xx}=V_{xx}/I_{xx} (longitudinal resistance) and R_{xy}=V_{xy}/I_{xx} (transverse resistance), with I_{xx} the injected dc current (100 μA) and V_{xx} and V_{xy} the voltages measured parallel and perpendicular to the injected current. The samples were measured using the 4-point technique. For Hall and magnetoresistivity measurements, magnetic fields were swept up to ± 14 T. The pure Hall signal, which is "odd" with respect to the applied field, was calculated as $\langle R_{xy}(H)\rangle$=(R_{xy}(+H)-R_{xy}(-H))/2. This allows us for remove any spurious contributions to R_{xy}. We calculated the resistivity ρ_{xx} and ρ_{xy} via the Van der Pauw method, ρ_{xx}=$R_{xx} \cdot \frac{\pi}{ln(2)} \cdot t$ and ρ_{xy}=$R_{xy} \cdot t$.

Magnetic characterization.

The materials were magnetically characterized using a superconducting quantum interference device (SQUID) in a Quantum Design Magnetic Properties Measurement System (MPMS) [&]. The temperature dependence of the magnetization was measured in 0.1 T magnetic field during a warming run after a field-cool or zero-field-cool procedure. The diamagnetic contribution of the substrate was removed by a linear fitting at high magnetic fields.

Magnetic Force Microscopy (MFM)

The MFM measurements were carried out using a LT NanoMagnetics [&] commercial microscope. Simultaneous magnetic and topographic images shown in this work were obtained at 17 K, in dynamic mode, using commercial tips from Nanosensors (PPP-MFMR) [&]. The retrace mode has been employed, acquiring topography during the first pass and MFM signal during the second pass at a set lift height of nominally 100 nm. Employing. The tip-sample magnetic interaction is recorded in this second pass by measuring the phase shift Δϕ of the oscillation of the cantilever with respect to the excitation as a function of the position. Images are rendered using WSXM software[62]

Polarized Neutron Reflectometry (PNR)

Samples were measured using the Magnetism Reflectometer (MR) of the Spallation Neutron Source at Oak Ridge National Laboratory and Polarized Beam Reflectometer (PBR) at the NIST Center for Neutron Scattering. Samples were field-cooled and measured in an in-plane field of 1 T and 0.68 T for MR and PBR, respectively, and 8 temperatures ranging between 20K to 300K. The data was analyzed by simultaneously fitting all the obtained reflectivities to models of the depth-dependent nuclear and magnetic scattering length densities, and using the GenX software[63,64] that is based on the Parratt formalism[65]. The PNR experiments were conducted on bilayer samples with small thickness (4- 5 nm) of the individual to ensure large interface sensitivity and allowed comparison with the x-ray absorption spectroscopy measurements (see our recent publication[44]). This sample

ARTICLE IN PRESS

structure did not allow obtaining reliable fits from x ray reflectivity measurements to compare with PNR fits. Reflectivity data measured at different temperatures were simultaneously fit to a model with temperature-dependent magnetic SLDs but a single nuclear SLD profile describing the sample allowing for a robust determination of the SLD profiles. The nuclear SLD profile showed sharp SIO/LSMO interfaces for both samples, with roughness appearing mostly at the top surface. An additional non-magnetic surface layer, with properties that varied with temperature, was necessarily included to account for surface contamination resulting from a slight vacuum leak of the closed cycle refrigerator holding the sample.

Magneto-optical Kerr effect (MOKE) microscopy

MOKE microscopy measurements were performed using a commercial wide-field MOKE microscope from EVICO MAGNETICS[&] . Samples were mounted within an optical cryostat cooled with liquid nitrogen, enabling measurements between 77 K and 300 K. A 4-pole magnet provided in-plane applied fields up to 175 mT. Images were taken using the longitudinal Kerr effect that is sensitive to the in-plane magnetization. The intensities over each set of 2x2 pixels were summed, reducing the total number of pixels by a factor of 4, in order to optimize the image contrast. Differential images were obtained by subtracting from the original image, an image taken while the sample was magnetically saturated. This is done to minimize image contrast from structural variations and maximize sensitivity to the Kerr effect contrast.

Acknowledgements

We acknowledge useful discussions with Nicolas Reyren and Vincent Cros. Work at UCM and Laboratoire Albert Fert supported by 2020 research and innovation program under the EIC pathfinder grant 101130224 "JOSEPHINE", and COST action "SUPERQUMAP". Work at UCM supported by Agencia Estatal de Investigación through PID2023-148884OB-I00, TED 2021-130196B-C21, and by and by "(MAD2D-CM)-UCM" project funded by Comunidad de Madrid, by the Recovery, Transformation and Resilience Plan, and by Next Generation EU from the European Union. Work at CNRS/Thales supported by French ANR "SUPERFAST. Work by S.G.E.t.V. and S.R. (neutron experiments and analysis) was supported by the U.S. Department of Energy, Office of Science, Basic Energy Sciences, Materials Sciences and Engineering Division. This research used resources at the Spallation Neutron Source, a DOE Office of Science User Facility operated by the Oak Ridge National Laboratory. Work at ICMM supported by the Ministry of Science, Innovation and Universities (Spain) through the projects PDC2023-145920-I00 and PID2023-151946OB-I00 and the Severo Ochoa Centres of Excellence program through Grant CEX2024-001445-S. J.J.R. acknowledges the Generation D initiative, promoted by Red.es, an organization attached to the Ministry for Digital Transformation and the Civil Service, for the attraction and retention of talent through grants and training contracts, financed by the Recovery, Transformation and Resilience Plan through the European Union's Next Generation funds.

Data availability statement. The raw data are available from the corresponding authors upon reasonable request.

Authors contributions. APS, SL, RF, FG, JT prepared the samples with help and guidance of CL, and JS. JJR, CM, FM, MGH did the MFM. MC did the STEM EELS microscopy. APS, RF, JT, FM and MGH did the SQUID measurements. APS did the transport experiments with supervision of ZS, CL and JS. SV did x ray absorption

ARTICLE IN PRESS

measurements. SGETV, TRC, BJK and SR did and analyzed the neutron measurements. SGETV did and analyzed the MOKE measurements. APS, CL, JEV, SGETV, JS analyzed the data. SGETV, JEV, JS wrote the manuscript with input and help of all authors.

Competing interests: The authors declare no competing interests.

ARTICLE IN PRESS